# Generation and Annealing of Crystalline Disorder in Laser Processing of Silicon

20

Mool C. Gupta, Leonid V. Zhigilei, Miao He, and Zeming Sun

## Contents



M. C. Gupta (✉)
Department of Electrical and Computer Engineering, University of Virginia, Charlottesville, VA, USA
e-mail: mgupta@virginia.edu; mg9re@virginia.edu

L. V. Zhigilei · M. He
Department of Materials Science and Engineering, University of Virginia, Charlottesville, VA, USA
e-mail: lz2n@virginia.edu; mh5wz@virginia.edu

Z. Sun
Department of Electrical and Computer Engineering, University of Virginia, Charlottesville, VA, USA

Cornell Laboratory of Accelerator-Based Sciences and Education, Cornell University, Ithaca, NY, USA
e-mail: zs253@cornell.edu



K. Sugioka (ed.), *Handbook of Laser Micro- and Nano-Engineering*,
https://doi.org/10.1007/978-3-030-63647-0_15

**Abstract**

The laser-induced crystalline disorder in silicon has attracted increasing interest due to its impact on the device performance of Si-based solar energy, optoelectronic, and electronic devices. Combined experimental and simulation approaches are effective for investigation of the fundamental mechanisms responsible for the formation of amorphous phase, polycrystalline structure, and crystal defects in the course of laser processing. In this chapter, the effects of laser pulse duration, wavelength, and fluence on the spatial distribution and concentration of point defects and dislocations, as well as the thickness and morphology of amorphous regions, are discussed based on the results of computer modeling and experiments. The laser-based thermal annealing is also considered as an effective technique for mitigating the laser-induced disorder. Overall, this chapter provides an up-to-date review of the disorder generation in laser-processed silicon and highlights the laser annealing technique for the disorder removal in silicon photovoltaic, optoelectronic, and electronic devices.

**Keywords**

Laser processing · Silicon · Crystalline disorder · Amorphous phase · Point defects · Dislocations · Photovoltaics · Laser annealing · Molecular dynamics simulations · Continuum modeling

## Introduction

The use of lasers in processing of silicon and other semiconductor materials has been experiencing rapid expansion owing to the increasing adoption of laser-based techniques in the fabrication of advanced photovoltaic, electronic, and optoelectronic devices. Lasers offer the ability to achieve noncontact localized surface treatment in material processing. Owing to these unique features, high-power laser processing becomes the solution to enable manufacturing of intricate device structures and yield cost-effective advantages (Sugioka et al. 2010). For example, laser ablation can facilitate the fabrication of interdigitated back contact (IBC) silicon solar cells by removing nanoscale surface layers while reducing the manufacturing cost through avoiding multiple patterning steps (Haase et al. 2018).

Recently, laser technology has experienced remarkable advances (Fig. 1a), especially in applications of lasers with ultrafast pulse duration and short wavelength (Cheng et al. 2013). One example of successful demonstration of ultrafast laser applications is the generation of periodic micro-texture on silicon surfaces (Bonse et al. 2012; Halbwax et al. 2008; Iyengar et al. 2011). Meanwhile, the demands for novel materials and high-performance devices (Fig. 1a) are driving the expansion of laser-based applications into new areas, such as laser-processed thin films for forming local contact opening or generating silicon surface passivation (Walter et al. 2015; Sun et al. 2018).

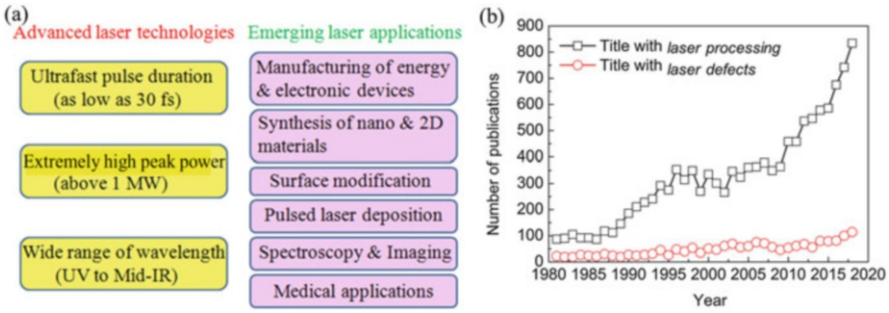


**Fig. 1** Fast development of laser technologies and applications is not matched by the corresponding growth in the number of investigations of laser-induced defect generation. (**a**) Chart showing advanced laser technologies and emerging laser applications. (**b**) Comparison between the number of articles with titles that include *laser processing* and *laser defects* from year 1980 to 2018 based on the Web of Science database

Laser processing has been widely studied for silicon device fabrication, including laser ablation, micro-texturing, doping, transfer of metal contacts, and annealing (Dahlinger et al. 2017). The major challenge, however, is presented by laser-induced structural disorder and defects, which can dramatically degrade the electrical properties of laser-processed silicon and negatively affect the performance of laser-based photovoltaic (Hameiri et al. 2010) and microelectronic (Arora and Dawar 1996) devices.

Table 1 summarizes various applications of laser processing in optoelectronic and electronic device fabrication, highlights the irradiation conditions that are suitable for these applications, and lists the corresponding types of the laser-induced disorder. A relatively clean material removal by laser ablation can be achieved by using short-pulse duration and ultraviolet (UV) wavelength lasers that minimize collateral damage and limit the extent of the heat-affected zone. Yet, the generation of amorphous phase and point defects can barely be avoided. The laser melting and doping are reliant on the thermal effect of laser irradiation, and a laser with nanosecond pulse duration is a typical option in this case. The unwanted presence of ablation, thermal stresses, and fast rate of the solidification can be responsible for the generation of amorphous phase and crystal defects in this regime. Laser annealing, at temperatures near the melting threshold, can be used to reduce or remove the laser-induced disorder. This effect can be achieved with longer, microsecond or millisecond, pulse durations.

As can be seen from Fig. 1b, the literature on laser-induced generation of structural disorder and crystal defects is limited as compared to the publications that discuss the laser processing research. Thus, this chapter intends to summarize the current experimental and computational studies of laser-induced structural transformation and defect generation in silicon and to provide a brief overview of methodology and approaches suitable for investigation of defects in laser-processed semiconductors in general.

**Table 1** Laser processes and conditions used for optoelectronic and electronic device fabrication

| Processing | Regimes | Preferred pulse duration | Preferred wavelength | Possible laser-induced disorder |
|---|---|---|---|---|
| Micro-texturing | Ablation | fs, ps, ns | UV | Amorphous phase, polycrystalline structure, point defects, dislocations, grain boundaries |
| Ablation of dielectrics atop semiconductor surfaces | | | | |
| Ablation of a-Si | | | | |
| Doping | Melting | ns, μs | Visible | |
| Transfer of metal contacts | Below melting threshold | | | |
| Annealing | | μs, ms | IR | Disorder removal |

## Laser-Induced Crystalline Disorder in Silicon: Experiments and Computer Modeling

Laser processing can induce crystalline disorder in silicon, mainly due to kinetic limitations during rapid melting and resolidification (Yater 1992). The timescale for generation of disordered metallic liquid phase under conditions of strong superheating created by the fast laser energy deposition is several picoseconds in the thermal melting regime, and it can be as fast as a few hundred femtoseconds when nonthermal melting mechanisms are activated by ultrafast pulses (Sokolowski-Tinten et al. 1995). Experiments identify the timescale of nonthermal disordering to be ~150 fs after the excitation by a 100 fs pulse (Shank et al. 1983; Tom et al. 1988). Computational studies further confirm the bond-breaking within ~200 fs after excitation by a 20 fs pulse and also determine the melting and ablation thresholds under incident pulses of different durations (Jeschke et al. 2002; Herrmann et al. 1998). Resulting from the rapid spatially localized heating, the high cooling rate can hardly produce perfect arrangement of atoms, as schematically shown in Fig. 2. As a result, the crystalline disorder, which disrupts the periodic crystal lattice, is generated in the form of amorphous phase or a high density of crystal defects.

The induced crystalline disorder is principally defined by the formation of amorphous phase or polycrystalline structure, as well as the generation of local structural defects, such as point defects, dislocations, and grain boundaries. In the amorphous silicon, the irregular arrangement of Si-Si bonds leads to the formation of tail energy states at the edge of conduction and valence bands; and the localized defects, especially dangling bonds, can cause the continuously distributed defect states. Similarly, the crystal defects in the single crystal silicon can also introduce the defect energy levels within the bandgap. These defect energy states function as the electron-hole recombination sites and limit the minority carrier lifetime (Ametowobla et al. 2012), increase leakage current (Young et al. 1982), and adversely affect device performance.

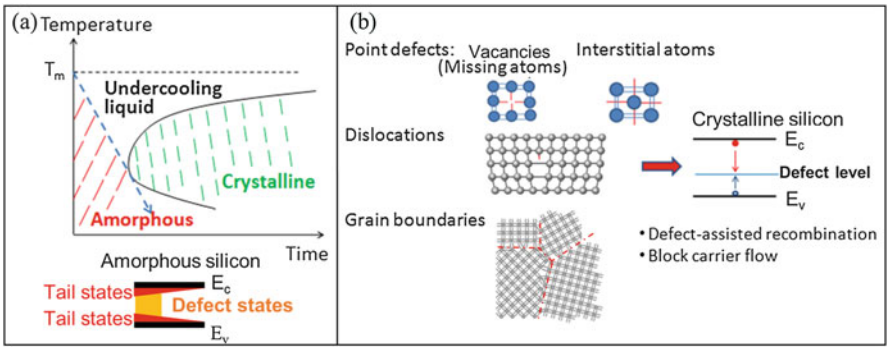


**Fig. 2** Different types of laser-induced disorder: (**a**) formation of amorphous phase and (**b**) crystal defects

The challenge for examining laser-induced disorder is the nonequilibrium nature of processes occurring during the resolidification, where the generation of defects at the rapidly advancing solidification front, nucleation of new crystallites, and thermal stresses all affect the final microstructure of the resolidified region. Correlating experimental observations with computational predictions is an effective method to reveal the fundamental mechanisms governing the disorder generation in laser-processed silicon. The following three sections will detail the state-of-the-art investigations.

## Experimental Studies on Laser-Induced Amorphous Phase in Silicon

The generation of the amorphous phase during laser processing of single crystal silicon has been observed in experiments since the 1970s (Tsu et al. 1979). Figure 3a illustrates the experimental setup for laser processing of silicon samples. The laser beam enters a galvanometer scanner and is focused on a silicon surface with a typical spot size of ~20 μm. A recent study (Crawford et al. 2008) using high-resolution scanning transmission electron microscopy (STEM) clearly imaged the laser-induced amorphous phase at the atomic scale (Fig. 3b). The short-range order in the amorphous regions is revealed in a selected-area diffraction pattern shown in Fig. 3c. In experiments, it is essential to understand the generation mechanisms of the amorphous phase under different laser conditions and identify laser parameters that can minimize the induced disorder, thus leading to superior device performance.

In this section, the physical properties of amorphous silicon and characterization techniques for determining the amorphous phase are reviewed. Three essential factors, including laser pulse duration, wavelength, and fluence, are discussed. In general, laser processing with short wavelength and short pulse duration can create a strong temperature gradient and induce rapid quenching of a transiently melted region in an irradiated sample, which is the required condition for amorphization. However, multiple additional factors can affect the amorphization process, and the

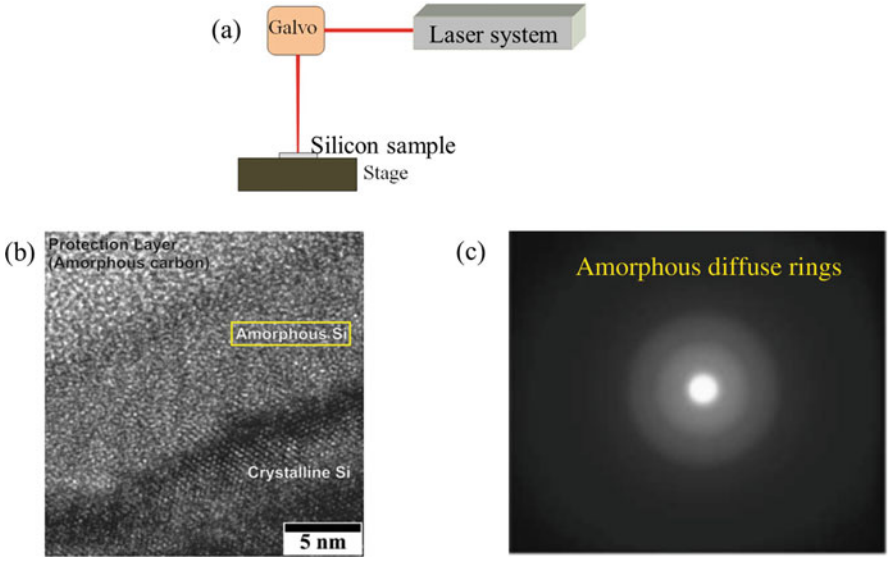


**Fig. 3** (**a**) Schematic of laser processing experimental setup. (**b**, **c**) Example of laser-induced amorphous phase generated by an 800 nm wavelength, 150 fs pulse duration laser. (Adapted from Crawford et al. (2008), with the permission of AIP Publishing). (**b**) Cross-sectional transmission electron microscopy (TEM) image from a sample processed by a single pulse at a laser fluence of 11 J/cm$^2$. (**c**) Diffraction pattern of amorphous phase produced after irradiation by five pulses at a laser fluence of 1.3 J/cm$^2$

observation of amorphous phase has been reported for different laser systems and in different irradiation regimes, e.g., in laser ablation regime.

## Physical Properties of Amorphous Silicon

Amorphous silicon is commonly represented by a continuous random network (CRN) model, but the structure of the real amorphous phase is not yet fully understood and can be strongly affected by the amorphization conditions. In the network, the a-Si atoms have short-range order with fourfold coordination and nearly constant bond length while lacking long-range order. The bond angle is distorted in the amorphous silicon as compared to the crystalline silicon, leading to a higher Gibbs free energy ($G$) as illustrated in Fig. 4a. Thompson et al. (1984) determined the melting temperature of amorphous silicon ($T_a$) to be ~250 K lower than that of the crystalline silicon ($T_m$). At an undercooling exceeding 250 K (i.e., at temperatures more than 250 K below $T_m$), the amorphous phase becomes thermodynamically more stable than the undercooled liquid silicon and can remain in the metastable state with respect to the equilibrium crystalline silicon due to the kinetically suppressed crystallization.

Stiffler et al. (1988) found that severe undercooling of ~500 K (0.7 of silicon melting temperature $T_m$) is a transition temperature for homogeneous crystalline silicon nucleation. The extreme undercooling is expected to favor amorphization,

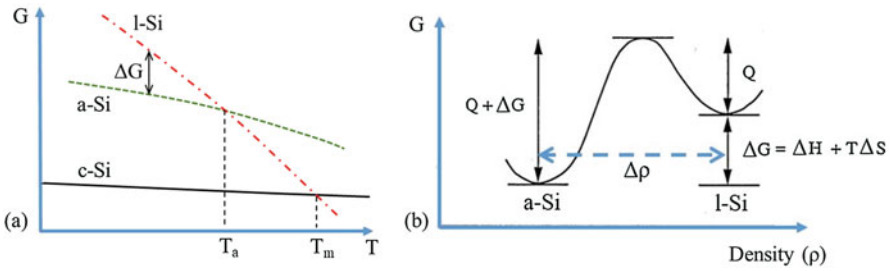


**Fig. 4** (**a**) Temperature dependence of the Gibbs free energies of liquid (l-Si), amorphous (a-Si), and crystal (c-Si) phases of Si and (**b**) diagram showing the activation energy (Q) and the density change (Δρ) for the liquid to amorphous phase transformation

but the amorphous silicon has not been observed until below 0.7 $T_m$. The reason is not fully clear yet. It is possibly due to a long incubation time for the amorphous phase formation from liquid or due to the remelting of any formed amorphous silicon with the subsequent *l*-Si to *c*-Si process. The liquid/solid interface movement involves the mobility of atoms at the interface, the covalent reordering, and density change. The density of amorphous silicon is 1.8% smaller than that of crystalline silicon, which, in turn, is 10% less dense than the liquid silicon (Custer et al. 1994). During the amorphization, the phase transformation not only involves overcoming the activation barrier (Q) but also needs to accommodate the density difference (Δρ), as schematically shown in Fig. 4b. In general, the temperature dependence of the interface velocity is the key to revealing the kinetics of the phase transformation, and this problem is addressed by simulations discussed in section "Multiscale Modeling of the Laser-Induced Formation of Amorphous State."

## Characterization of Laser-Induced Disorder

Electron microscopy is the most direct and definite approach to determine the laser-induced disorder. Electron diffraction performed in transmission electron microscope (TEM) can reveal the characteristic diffraction patterns with diffuse rings (e.g., Fig. 3c), which suggests the absence of long-range order in the atomic positions and confirms generation of amorphous phase.

X-ray diffraction and spectroscopies can also be used to detect the presence of disorder phases. Amorphous or poorly ordered phases eliminate the distinctive X-ray diffraction peaks or, in partially amorphized regions, broaden the width of the crystalline diffraction peak. Raman spectroscopy is widely used for studying the disorder in silicon lattice (Bonse et al. 2004). A broad Raman peak at ~480 $cm^{-1}$ wave number appears as an evidence of amorphous silicon. Due to the low amounts of amorphous phase typically present in the surface region of laser-processed samples, the crystalline silicon peak is barely avoided, and the amorphous silicon peak may not be prominent. Instead, the presence of amorphous silicon can be characterized by studying the full-width-at-half-maximum (FWHM) value of the crystalline silicon peak (Fig. 5a). Photoluminescence (PL) spectroscopy is another effective technique to evaluate the crystal quality by checking the band-edge

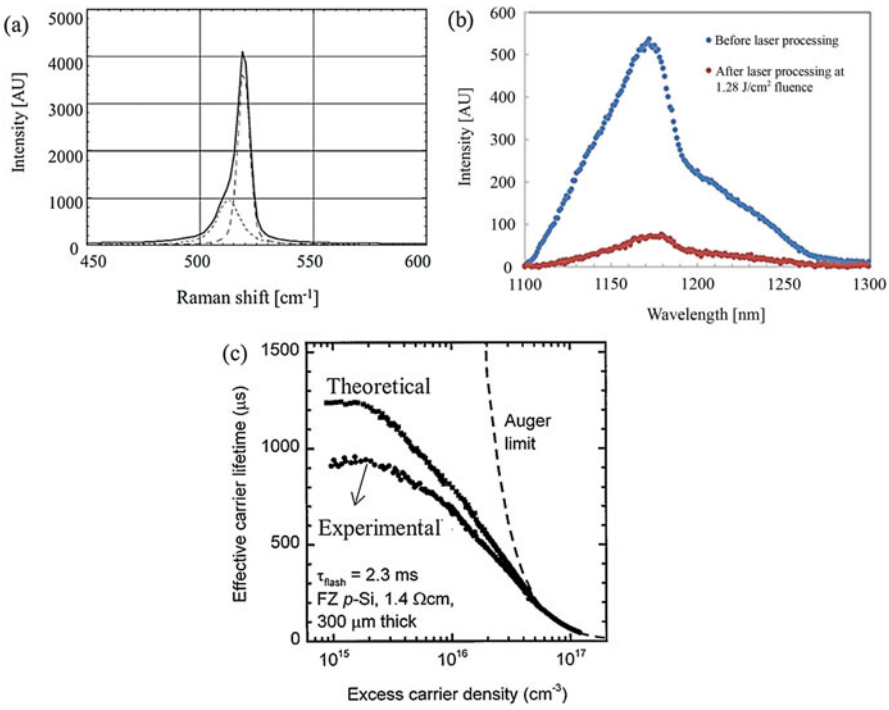


**Fig. 5** Characterization techniques for revealing the laser-induced disorder. (**a**) Raman spectroscopy: broadening of the c-Si peak at laser-processed spot. (Adapted from Amer et al. (2005), with permission from Elsevier). (**b**) Photoluminescence spectroscopy: comparing band-edge emission between bare silicon wafer and laser-processed silicon. (Reprinted from Sun and Gupta (2018a), with the permission of AIP Publishing). (**c**) Photoconductance decay measurement: the extracted carrier lifetime as an indicator of crystal quality. (Reprinted from Nagel et al. (1999), with the permission of AIP Publishing)

emission (Fig. 5b). Moreover, the crystalline quality can also be revealed by measuring the surface electrical properties. Charge carrier lifetime extracted from the photoconductance decay is a critical parameter to evaluate time duration before the carriers are trapped in states created by the disorder (Fig. 5c).

## Effect of Laser Pulse Duration

Investigations using femtosecond (Amer et al. 2005; Bonse et al. 2002; Crouch et al. 2004; Jia et al. 2004), picosecond (Liu et al. 1981), and nanosecond (Tsu et al. 1979; Amer et al. 2005; Crouch et al. 2004; Sun and Gupta 2018b) laser systems have all reported the amorphization of the c-Si surface after the laser processing. It is necessary to clarify the laser modification regimes, including but not limited to melting and ablation (removal of material). In the regime of surface melting and resolidification, the amorphization occurs only at short pulse durations. In experiments, the threshold values are determined to be 100 ps for 600 nm wavelength pulses and 3 ns for 300 nm wavelength pulses (Yater 1992). The simulations predict

a pulse duration threshold of 90 ps for 532 nm laser wavelength (see details in section "Multiscale Modeling of the Laser-Induced Formation of Amorphous State"). Above the threshold pulse duration, the formation of the amorphous phase can be suppressed in the melting regime due to the relatively low-temperature gradients suitable for crystallization. In contrast, laser ablation causes a complicated physical scenario that is not yet fully understood. In the ablation regime, the amorphous phase generation via laser processing with pulse durations of 30–50 ns has been widely reported (Amer et al. 2005; Crouch et al. 2004; Sun and Gupta 2018b). Laser ablation is essential to many practical laser-enabled applications. Thus, it is barely possible to avoid the disordered phases by simply selecting an appropriate melting regime for laser processing.

In the laser ablation regime, Amer et al. (2005) compared the average amorphization ratio between femtosecond and nanosecond laser-processed samples (Fig. 6). At laser fluences below 10 J/cm$^2$, which most manufacturing processes apply to silicon devices, femtosecond laser processing induces more extensive amorphization than nanosecond laser processing. Moreover, the degree of amorphization, quantified by the relative integrated intensity of the a-Si peak in the Raman spectra, remains high for all femtosecond laser fluences studied, while it gradually increases with fluence in the nanosecond laser processing, especially at fluences below 10 J/cm$^2$. A similar observation was reported by Crouch et al. (2004), who compared the laser micro-textured silicon produced by femtosecond and nanosecond laser systems. The below bandgap absorption is much higher for femtosecond micro-textured silicon, which is characterized by highly disordered structures. Indeed, the processing by femtosecond pulses tends to induce larger amount of disorder in silicon even in the laser ablation regime.

Nevertheless, the absence of an amorphous phase in the femtosecond laser ablation is possible and has been reported by Rogers et al. (2009). The mechanism is similar to the retention of crystallinity in nanosecond laser ablation (Sun and

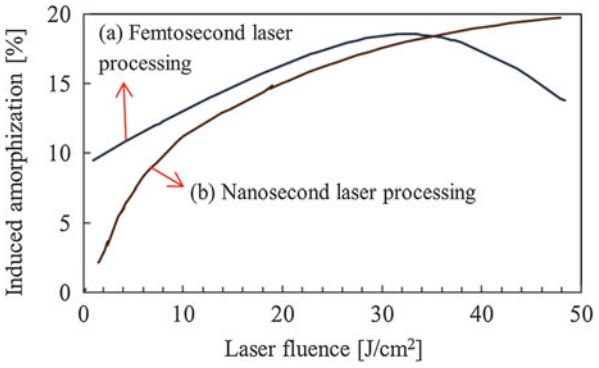


**Fig. 6** Comparison of average induced amorphization as a function of laser fluence between (a) 150 fs and (b) 30 ns pulse laser processing. (Adapted from Amer et al. (2005), with permission from Elsevier)

Gupta 2018b), where the final surfaces are cleaned from any possible amorphous regions by the strong ablation process. Further discussion of the effect of ablation on surface amorphization can be found below in the subsection on the effect of laser fluence.

### Effect of Laser Wavelength

Wavelength is an important parameter that defines the laser absorption depth in silicon and thus the temperature profile in the heated region. As shown in Fig. 7a, the absorption depth significantly drops with wavelength, and UV light is mostly absorbed within a depth of about 10 nm. In the melting regime, the UV wavelength pulse, due to strong surface heating, can increase the pulse duration threshold for amorphization to the nanosecond range. Tsu et al. (1979) have observed the formation of a disordered phase upon irradiation by a 10 ns laser pulse at a wavelength of 266 nm. The shallow absorption depth ($<$10 nm) at this wavelength leads to a cooling rate above $10^{11}$ K/s, which is one order of magnitude higher than the rate of $5 \times 10^9$ K/s, below which the crystallization can take place (Tsu et al. 1979; Thompson et al. 1983). Note that the cooling rate required for the onset of crystallization determined in experiments is commonly an average value based on photocurrent measurements at a timescale beyond 1 ns (Thompson et al. 1983), whereas simulation studies overcome the time limitation of the experiments and further confirm that the cooling rate has to be below $10^{12}$ K/s (see section "Multiscale Modeling of the Laser-Induced Formation of Amorphous State").

In the ablation regime, Lu et al. (2008) compared the ablation depth, or the depth of craters, produced by UV (266 nm), visible (532 nm), and IR (1064 nm) wavelength pulses (Fig. 7b). The laser ablation thresholds are dramatically decreased when using a shorter wavelength pulse, and the ablation depth observed in the IR laser processing is the lowest.

The strong wavelength dependence of the ablation behavior has direct implications for the structural disorder. A recent work (Sun and Gupta 2018b) investigating silicon ablated by 1064 nm and 532 nm wavelength nanosecond pulses demonstrates the retention of single-crystalline phase in strong ablation by the short-wavelength pulse (Fig. 8a) and formation of amorphous and polycrystalline phases in ablation by a long-wavelength pulse. As shown in Fig. 8b, the ablated material could be redeposited on the laser-processed surface in an amorphous particulate state (Tsu et al. 1979; Sun and Gupta 2018b).

### Effect of Laser Fluence

Computational studies (section "Multiscale Modeling of the Laser-Induced Formation of Amorphous State") suggest that the generation of crystalline disorder, i.e., amorphous structure, can be controlled by adjusting laser fluence. In the melting regime, relatively high laser fluence can decrease the cooling rate and result in the epitaxial regrowth of the crystalline phase during the resolidification. To a certain extent, this prediction is also valid when laser ablation occurs.

Bonse et al. (2002) illustrated the physical processes occurring in different regions of a single fs pulse-processed spot (Fig. 9a). With a Gaussian profile of laser fluence distribution, the low local fluence at the outer region tends to generate an amorphous phase, while the high local fluence in the inner region produces an

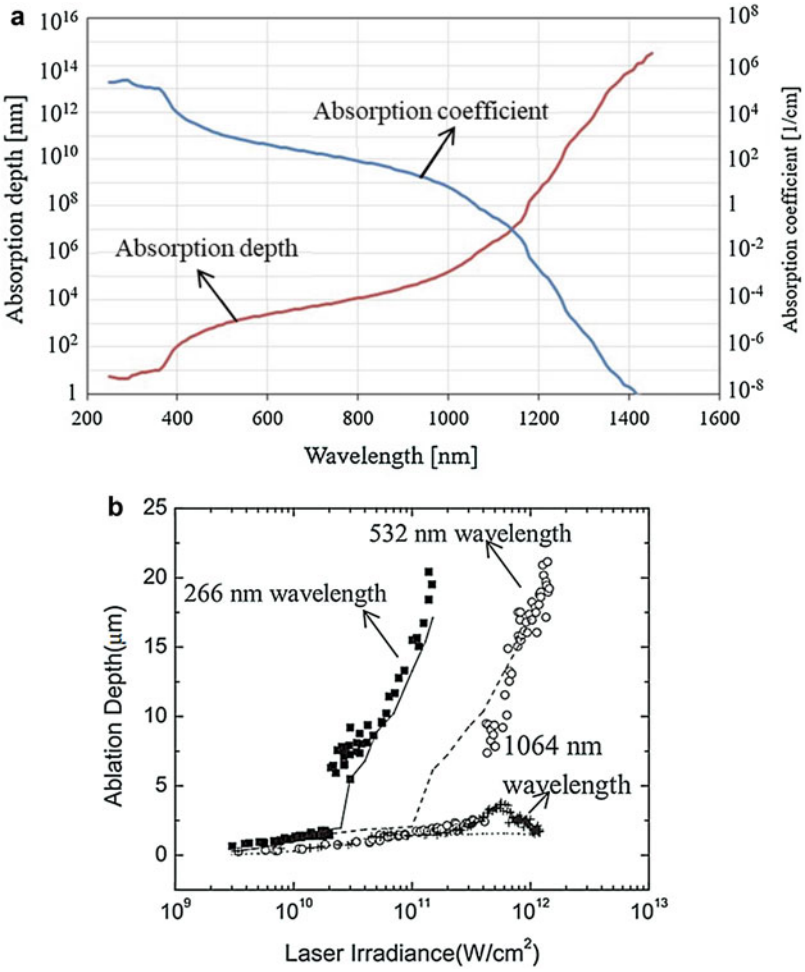


**Fig. 7** (**a**) Silicon absorption depth and corresponding absorption coefficient as a function of incident light wavelength plotted based on data reported in Green (2008). (**b**) Comparison of ablation depth as a function of laser irradiance observed in 266, 532, and 1064 nm wavelength laser processing. (Adapted from Lu et al. (2008), with the permission of AIP Publishing). Pulse duration was fixed at 3 ns

annealing effect that favors crystallization. Increasing the laser fluence of a single pulse or applying multiple pulses can cause morphological changes together with melting and ablation. Relatively high laser fluence with a single or a few pulse irradiation (Region 1 in Fig. 9b) can avoid a dramatic change in surface morphology while achieving the crystalline phase.

Another observation is that high laser fluences can cause ablation and feasibly generate a clean surface. Strong ablation at extremely high fluences and irradiation by multiple pulses (Region 2 in Fig. 9b) can also attain a crystalline surface. This is

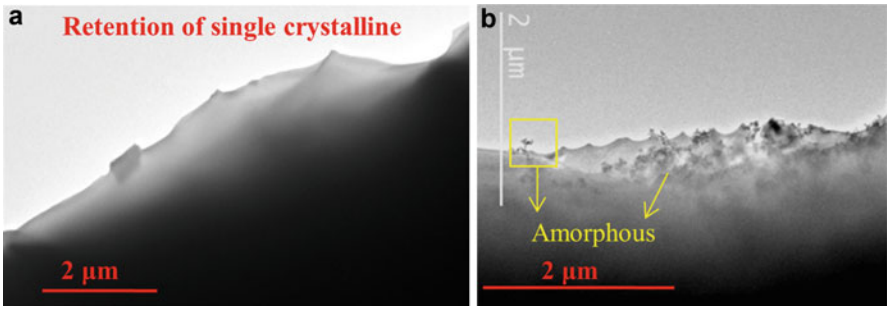


**Fig. 8** (**a**) Retention of single-crystalline phase and (**b**) redeposition of amorphous nanoparticles in laser ablation at laser fluences of 1.64 J/cm$^2$ and 1.31 J/cm$^2$, respectively. The experiments are performed at a laser wavelength of 532 nm and a pulse duration of 1 ns. (Adapted from Sun and Gupta (2018b), with permission from Elsevier)

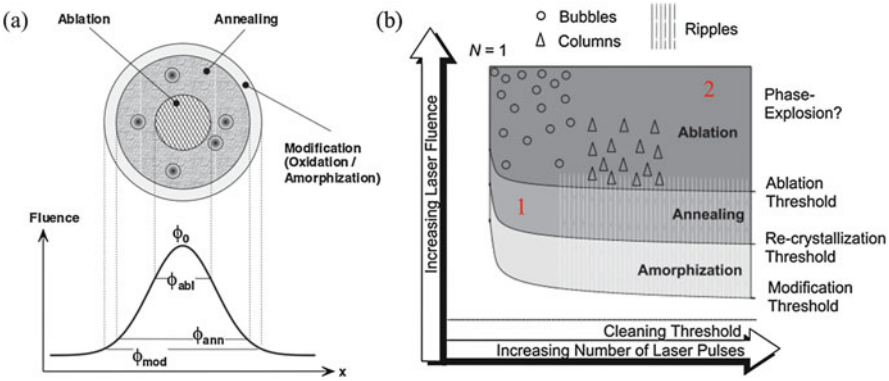


**Fig. 9** Effect of laser fluence on ablation and amorphous phase generation in femtosecond laser processing. (Adapted from Bonse et al. (2002), with permission from Springer Nature). (**a**) Physical processes occurring at different locations of a laser-processed spot with the Gaussian distribution of laser fluence. (**b**) Schematic showing physical and morphological phenomena at various laser fluences and pulse numbers

especially true for short-wavelength lasers which can easily produce strong ablation (Fig. 7). Taking advantage of this mechanism, single-crystalline silicon is not only retained using nanosecond pulses (Fig. 8a) but also observed after irradiation by femtosecond pulses (Rogers et al. 2009).

## Multiscale Modeling of the Laser-Induced Formation of Amorphous State

Section "Experimental Studies on Laser-Induced Amorphous Phase in Silicon" has provided a brief overview of the formation of amorphous structure in Si targets

irradiated at the different laser wavelengths, pulse durations, and fluences. However, experimental probing of the ultrafast laser-induced processes in the shallow laser-modified region, which take place on femtosecond to nanosecond timescales and sub-micrometer length scales, remains challenging. Moreover, the relationships between numerous nonequilibrium processes involved in the laser-material interactions and overlapping in time and space, such as rapid melting and resolidification, fast cooling leading to amorphization, and generation of crystal defects, are unlikely to be completely uncovered based on experimental data alone.

Numerical modeling of the laser-induced phase and structural transformations provides a valuable tool for understanding the fundamental mechanisms responsible for the modification of silicon structure by laser irradiation. In particular, the ability of short-pulse laser irradiation to produce high density of point defects, dislocations, and stable amorphous structure has been investigated in molecular dynamics (MD) simulations for a variety of materials (Thompson et al. 1983; Lin et al. 2008; He et al. 2019; Yang et al. 2012; Shugaev et al. 2018). The MD technique is capable of resolving complex processes on atomic scale but comes at the price of high computational cost. In order to describe the laser-induced processes at experimental timescales and length scales, computationally efficient continuum simulations are usually adopted (Shugaev et al. 2018; Kisdarjono et al. 2003; Bulgakova et al. 2005).

In this section, an advanced computational method is introduced, which enables the integration of the predictive power of both atomistic and continuum simulations into a multiscale model. In this method, the kinetics and mechanisms of laser-induced phase and structural transformations are first revealed by atomistic simulations. The results of the atomistic simulations then serve as the basis for the design and parameterization of an advanced continuum-level model, so that the computational predictions can be directly mapped to experimental observations and used for optimization of laser processing conditions in practical applications.

### Molecular Dynamics Study of Solid-Liquid Phase Transformations

In MD modeling, the only input is the description of interatomic interactions, and no assumptions are required for the processes or mechanisms under study, thus making it well suited for exploring the kinetics of nonequilibrium processes (e.g., melting/solidification under conditions of overheating/undercooling) and revealing new physical phenomena (e.g., establishing the mechanisms responsible for the generation of crystal defects). Figure 10 shows two examples illustrating the application of MD simulations to address the conditions for amorphization and the temperature dependence of the movement of the solid-liquid interface.

The transition of the undercooled Si from liquid into amorphous state is illustrated in Fig. 10a, b, which show the results from a series of MD simulations of rapid cooling of a liquid Si system at different cooling rates (cr) (Zhang et al. 2015). The temperature dependence of the number density of atoms (Fig. 10a) indicates a structural change between 1000 K and 1500 K, since amorphous silicon is less dense than liquid silicon. This abrupt transition to a low-density state coincides with the change of temperature dependence of the Abraham ratio $R = g_{min}/g_{max}$, where $g_{min}$ and $g_{max}$ are the magnitudes of the pair correlation function at the first minimum and first maximum, respectively. The Abraham ratio is commonly used to

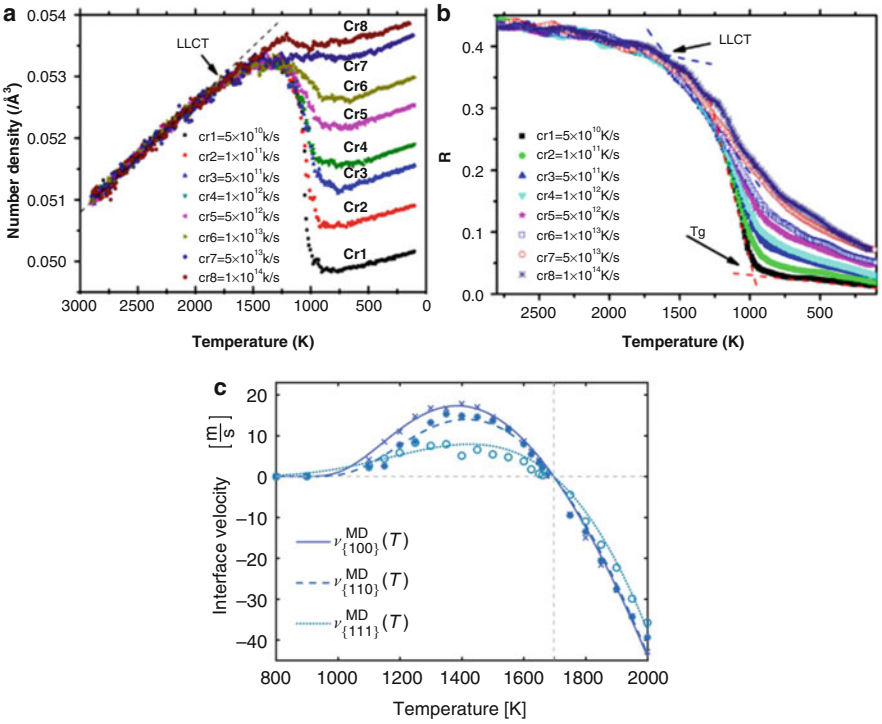


**Fig. 10** The temperature dependence of the number density (**a**) and Abraham ratio (**b**) of liquid/amorphous Si calculated in MD simulations of cooling of liquid Si performed with different cooling rates. The Abraham ratio R is calculated based on pair correlation function and is defined as $R = g_{min}/g_{max}$, where $g_{min}$ and $g_{max}$ are the magnitudes of the pair correlation function at the first minimum and first maximum, respectively. (**c**) Velocities of the crystal-liquid interfaces with different crystallographic orientations as functions of temperature predicted in MD simulations of a crystal-liquid coexistence Si system under constant temperature and zero pressure. (The figures in (**a**, **b**) are adapted from Zhang et al. (2015) and the figure in (**c**) is adapted from Bergmann et al. (2017))

characterize the structural transition from undercooled liquid into amorphous state (Sastry and Angell 2003; Jakse and Pasturel 2007). The temperature below which a stable amorphous structure is formed is identified as the amorphous transition temperature, $T_g$.

In addition to the conditions for the formation of amorphous structure, MD simulations can also be applied to predict the velocity of the solid-liquid interface as a function of temperature. As shown in Fig. 10c, the velocities of the crystal-liquid interface with different crystallographic orientations are evaluated from a series of crystal-liquid coexistence simulations performed at different temperatures (Bergmann et al. 2017). The {111} interface has the smallest velocity compared to the other two orientations, which is related to its densely packed structure and absence of favorable sites for the attachment of additional atoms on a {111} crystal

face. The MD predictions of the temperature-dependent interfacial velocities can be used for parameterization of kinetic equations that describe the propagation of melting/solidification front, e.g., Eq. 2 discussed below, in the section on continuum-level modeling.

## Continuum Modeling of Amorphization in the Course of Laser-Induced Melting and Resolidification

The direct MD simulation of processes occurring on the scale of an entire laser spot with a typical diameter of tens to hundreds of micrometers is clearly out of reach even with the most powerful modern supercomputers. Nevertheless, some of the predictions of MD simulations, such as the temperature dependence of the velocity of solid-liquid interface, types and densities of crystal defects generated in the course of rapid melting and resolidification, etc., can be used in the design and parameterization of large-scale continuum-level model. Traditional continuum-level description of thermal processes in laser-material interactions is based on the numerical solution of the heat diffusion equation complemented by source terms accounting for the laser energy deposition and latent heat of phase transformations:

$$\rho C_P \frac{\partial T}{\partial t} = \nabla \cdot (K_{th} \nabla T) + S_{\text{laser}} - S_m - S_e, \tag{1}$$

where $\rho$, $C_P$, and $K_{th}$ are density, heat capacity, and thermal conductivity of the target material, respectively. The three source terms on the right side of Eq. 1 represent the thermal energy sources/sinks due to the laser energy deposition $S_{\text{laser}}$, the release/absorption of heat at melting/resolidification front $S_m$, and the energy loss through vaporization from the surface of the irradiated target $S_e$.

In the description of laser-induced melting and resolidification, a simple phase-change model based on conventional assumptions of local equilibrium at the solid-liquid interface (Wood 1981; Vonatsos and Pantelis 2005) is not suitable for the conditions created by short-pulse laser irradiation, where strong temperature gradients are created, and fast thermal energy flow to/from the solid-liquid interface can lead to significant superheating/undercooling at the melting/solidification front. Therefore, a nonequilibrium kinetic description (Gupta et al. 1995; Jackson 2002; Kisdarjono et al. 2003), in which the instantaneous velocity of the solid-liquid interface is defined by local temperature at the interface, is needed for a realistic representation of the movement of the solid-liquid interface:

$$V_{sl}(T_{sl}) = V_0(T_{sl}) \left[ 1 - \exp\left( -\frac{\Delta G(T_{sl})}{k_B T_{sl}} \right) \right], \tag{2}$$

where $T_{sl}$ is the temperature at the solid-liquid interface, $V_0$ is a pre-factor related to the self-diffusivity in the liquid phase, and $\Delta G$ is the difference in Gibbs free energy between the liquid and solid phases. At moderate deviations from the equilibrium melting temperature $T_m$, the free energy difference can be approximated as $\Delta G(T_{sl}) \approx \Delta H_m(T_{sl})(1 - T_{sl}/T_m)$, where $\Delta H_m$ is the latent heat of the solid-liquid

phase transformation. As discussed above, the pre-factor $V_0$ can be fitted to the results of a series of solid-liquid coexistence atomistic simulations performed at different temperatures.

As an example of the application of the multiscale model for investigation of the laser-induced formation of amorphous structure, Fig. 11 illustrates the results of 1D simulations of a Si target under different laser irradiation conditions in the regime of melting and solidification. The glass transition temperature $T_g = 0.71\ T_m$ is predicted in MD simulations, which is close to the value determined in Fig. 10b. As shown in Fig. 11a, b, the resolidification of the laser-melted region proceeds through the propagation of the solid-liquid interface under conditions of fast cooling. When the undercooling level for amorphization is achieved at the solidification front, the front stops, and the remaining undercooled liquid transforms into a stable amorphous phase. The maximum melting depth increases with laser fluence, resulting in a larger depth of the liquid region that may potentially be frozen into the amorphous state. This effect is counteracted by the decrease of the cooling rate with increasing fluence, which retains the solidification front at elevated temperature, thus suppressing the formation of amorphous structure. The fluence dependence of the thickness of the amorphous region formed by laser irradiation with different pulse durations is illustrated in Fig. 12a, which has similar trend as Fig. 6a. Based on the above discussion, the formation of a ring-shaped amorphous region in the Si target shown in Fig. 9a can be explained as follows: At the laser spot center, the local laser fluence exceeds the threshold fluence that ensures sufficient cooling rate to induce the transition to the amorphous state. Conditions for amorphization can only be achieved at lower local fluences at the periphery of the Gaussian laser profile, leading

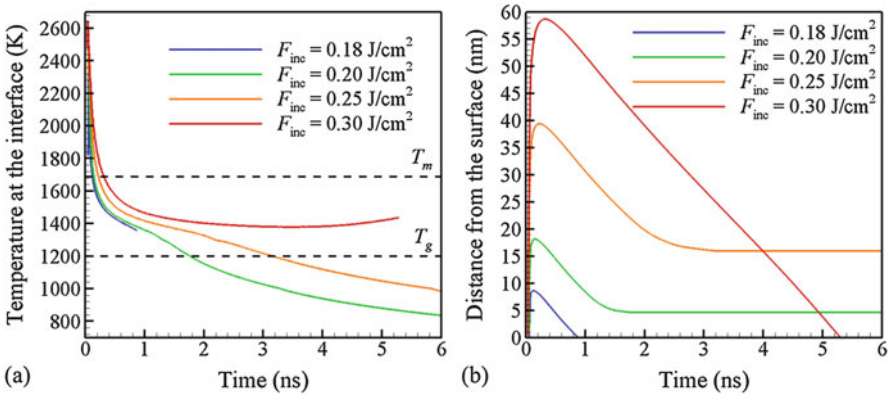


**Fig. 11** The evolution of temperature (**a**) and depth (**b**) of the crystal-liquid/amorphous interface predicted in 1D continuum simulations of a Si target irradiated by a 30 ps laser pulse at different fluences. The laser wavelength is 532 nm. In (**a**), $T_m$ and $T_g$ mark the melting temperature (1687 K) and the glass transition temperature, respectively. The termination of the profiles for $F_{inc} = 0.18$ J/cm$^2$ and $F_{inc} = 0.30$ J/cm$^2$ in (**a**) indicates the complete crystal regrowth with the solidification front reaching the target surface. (The figures are adapted from He and Zhigilei in preparation)

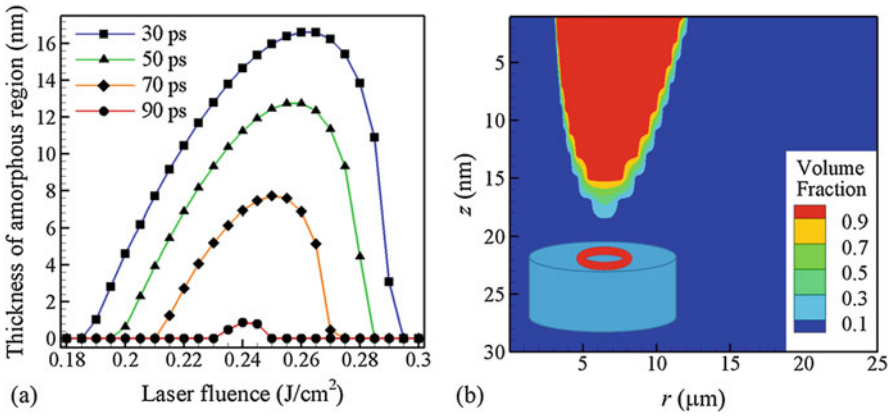


**Fig. 12** (**a**) Prediction of the depth of amorphous region as a function of incident laser fluence from 1D continuum simulations of laser irradiation of Si with different pulse durations and a wavelength of 532 nm. (**b**) Contour plot of the volume fraction of amorphous phase in a Si target predicted in a 2D continuum simulation performed with a Gaussian laser beam profile. The laser fluence is 0.3 J/cm$^2$, the pulse duration is 30 ps, the spot diameter defined as the full width at 1/e$^2$ height of the Gaussian profile is 50 μm, and the laser wavelength is 532 nm. The inset illustrates the ring-shaped morphology of the amorphous region marked by red color. (The figures are adapted from He and Zhigilei, in preparation)

to the formation of a ring-shaped amorphous structure surrounding the fully crystallized central part. This scenario is demonstrated in 2D continuum simulations with cylindrical symmetry, and the volume fraction of amorphous phase after laser irradiation is plotted in Fig. 12b.

## Experimental and Computational Investigations of Laser-Induced Generation of Structural Defects in Silicon

Laser-induced structural defects, such as point defects, oxygen impurities, and dislocations, can locally disrupt the crystal lattice periodicity. Although the long-range order of the silicon crystal still exists in the presence of laser-induced structural defects, the electrical properties of silicon and the device performance have been shown to undergo dramatic degradation. It is necessary, therefore, to include the discussion of crystal defects within the context of the laser-induced generation of structural disorder.

### Experimental Observations

In experiments, progress on laser-induced damage investigation has been made owing to the advances of atomic-level characterization techniques. Previous studies (Mooney et al. 1978) identified the energy levels of induced defects in the silicon bandgap. Together with the emergence of laser-processing techniques for silicon-based energy applications, the research has recently focused on the evaluation of

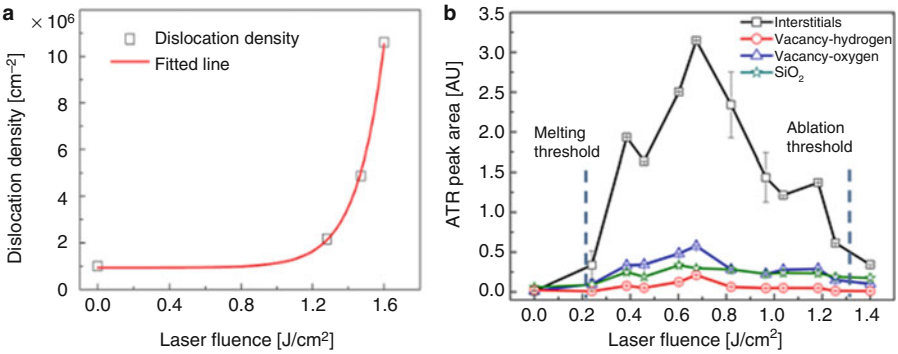


**Fig. 13** Dislocation and point-defect quantification studies performed with (**a**) 1064 nm wavelength, 50 ns pulse duration and (**b**) 532 nm wavelength, 1 ns pulse duration lasers, respectively. The laser-induced dislocation density shown in (**a**) is determined by counting chemical etch pits. (Reprinted from Sun and Gupta (2018a), with the permission of AIP Publishing). The ATR (attenuated total reflectance) point-defect peak area in (**b**) is used as an indicator of the point-defect concentration (Sun et al. in preparation)

performance degradation for solar cell devices due to the induced defects. Hameiri et al. (2010) and Ohmer et al. (2011) explored the minimization of defect formation in the laser doping technique by designing the device structure with a double $SiO_2$/$SiN_x$ stack and exploiting a line-focused laser beam, respectively.

A quantitative profile of defect density is of high interest in order to assess the impact of laser-induced defects on device performance and identify the irradiation conditions that minimize the generation of crystal defects. Recent studies (Sun and Gupta 2018a) find that the dislocation density is limited at laser fluences below the ablation threshold and increases nearly exponentially above the threshold (Fig. 13a). The laser-induced point defects (Sun et al. in preparation), however, exhibit very low concentrations at laser fluences either below the melting threshold or above the ablation threshold (Fig. 13b). A maximum in the point-defect concentration is observed between the two thresholds. The interstitials and vacancies (hydrogen-vacancy and oxygen-vacancy complexes) display similar behaviors. The mechanisms responsible for this non-monotonous laser fluence dependence are revealed in simulations discussed below.

## Modeling of Generation of Point Defects by Laser-Induced Melting and Resolidification

MD simulations have been widely used to provide the atomic-level insights into the kinetics of epitaxial crystal growth and formation of crystal defects at the solid-liquid interface (Luedtke et al. 1988; Ishimaru et al. 1998; Bernstein et al. 2000; Nishihira and Motooka 2002; Motooka et al. 2006; Chang et al. 2018), which is related to the rapid advancement of solidification front under conditions of strong undercooling. Figure 14 shows the results from a series of MD simulations of a Si solid-liquid

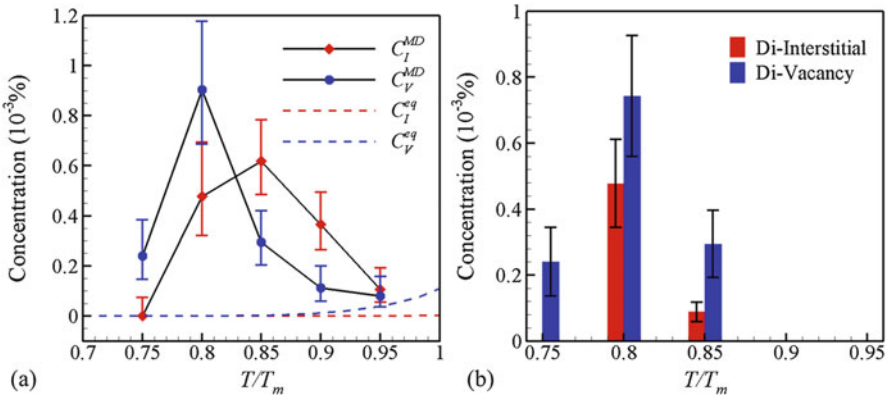


**Fig. 14** The results of the analysis of crystal defects generated in MD simulations of solidification proceeding by epitaxial crystal growth at different levels of undercooling. Temperature dependence of concentrations of individual interstitials (red squares) and vacancies (blue circles) is shown in at.% (**a**). The concentrations of di-interstitials (red bars) and di-vacancies (blue bars) are shown in (**b**). The results are averaged over four simulations performed under the same conditions. In (**a**), error bars are calculated as the range with 68% confidence assuming a Poisson distribution of point defects; in (**b**), error bars are calculated as the standard deviation of the mean. Predictions of equilibrium concentrations of interstitials and vacancies from Sinno et al. (1996) are shown in (**a**) as red and blue dashed lines, respectively. (The figures are adapted from Sun et al. in preparation)

coexistence system performed at different undercooling levels and zero pressure (Sun et al. in preparation). Such simulations have a computational setup similar to that described in section "Multiscale Modeling of the Laser-Induced Formation of Amorphous State," where the MD simulations were used to predict the temperature dependence of the solid-liquid interface velocities, e.g., Fig. 10c. The analysis of the resolidified part of the computational system reveals that a substantial number of individual point defects and their clusters are generated at the solidification front. The concentrations of individual point defects are averaged over four independent simulations performed for (001) orientation of the solid-liquid interface and the same undercooling conditions and are plotted as a function of temperature in Fig. 14. As compared to the equilibrium point defect concentrations calculated using the parameters provided in Sinno et al. (1996) and shown by the dashed lines in Fig. 14a, strong supersaturations of the interstitials and vacancies produced in the resolidified region are demonstrated.

The MD predictions of the concentration of point defects (vacancies and interstitials) generated during rapid solidification can be used to parameterize a continuum model capable of describing the distribution of point defects in the laser-melted target (Sun et al. in preparation). The continuum-level thermal model discussed in section "Multiscale Modeling of the Laser-Induced Formation of Amorphous State" is complemented with the following equations accounting for the generation, diffusion, and recombination of vacancies and interstitials in the irradiated target:

$$\frac{\partial C_I}{\partial t} = \nabla \cdot (D_I \nabla C_I) - R_{I,V} - R_{I,V_2} + S_I, \tag{3}$$

$$\frac{\partial C_V}{\partial t} = \nabla \cdot (D_V \nabla C_V) - R_{I,V} - 2R_{V,V} + R_{I,V_2} + S_V, \tag{4}$$

$$\frac{\partial C_{V_2}}{\partial t} = \nabla \cdot (D_{V_2} \nabla C_{V_2}) + R_{V,V} - R_{I,V_2} + S_{V_2}, \tag{5}$$

where $C_I$, $C_V$, and $C_{V_2}$ denote the instantaneous concentrations of single interstitials, single vacancies, and di-vacancies, respectively, and $D_I$, $D_V$, and $D_{V_2}$ are their temperature-dependent diffusion coefficients. $R_{I,V}$, $R_{I,V_2}$, and $R_{V,V}$ are the terms associated with reactions between different types of point defects, describing the annihilation of an interstitial and a vacancy, the combination of a single interstitial and a di-vacancy creating a single vacancy, and the formation of a di-vacancy from two individual vacancies, respectively. The source terms describing the generation of nonequilibrium interstitials and vacancies at the propagating solidification front, $S_I$, $S_V$, and $S_{V_2}$, can be parameterized based on the results of the atomistic simulations, similar to those shown in Fig. 14.

The ability of the multiscale modeling to predict the generation of point defects in the course of laser-induced melting and resolidification is exemplified in Fig. 15, which shows the concentration of interstitials and vacancies generated in a silicon target by a nanosecond laser pulse. In contrast to the simulation of picosecond laser irradiation discussed in section "Multiscale Modeling of the Laser-Induced Formation of Amorphous State," the irradiation by a longer, 1 ns, laser pulse reduces the cooling rate and does not result in the formation of the amorphous phase. The undercooling in the vicinity of the solidification front, however, leads to the formation of distinct regions of strong supersaturation of both vacancies and interstitials in the surface region that experiences transient melting and resolidification. At a later

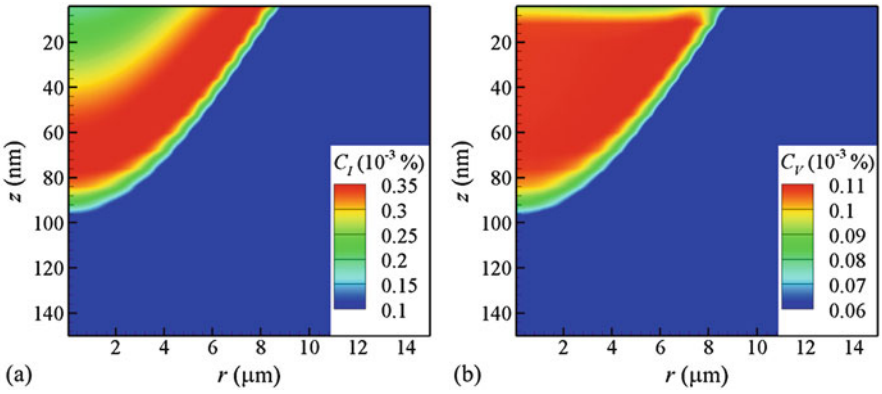


**Fig. 15** Spatial distributions of interstitials (**a**) and vacancies (**b**) produced in the surface region of a silicon target irradiated by a 1 ns laser pulse at a fluence of 0.45 J/m$^2$. The scale is shown in units of atomic percent. (The figures are adapted from Sun et al. in preparation)

stage of the solidification process, the interfacial temperature increases from 0.91 to 0.95 $T_m$ due to release of the latent heat, resulting in decreasing levels of vacancy and interstitial concentrations.

The multiscale modeling has also been successfully applied to explain the laser fluence dependence of point defect concentration observed in experiments (Fig. 13b). Figure 16 illustrates the results of the continuum-level simulations of laser irradiation of a Si target at different fluences, showing the evolution of the temperature at the solid-liquid interface as well as the concentration of point defects averaged over the transiently melted region. As shown in Fig. 16a, the solid-liquid interface undergoes rapid cooling at the beginning of the solidification process, followed by an increase of the interfacial temperature due to the release of latent heat. The temperature at the solidification front ranges from 0.9 $T_m$ to $T_m$, and, according to Fig. 14a, the densities of both individual interstitials and vacancies can be expected to decrease with increasing interfacial temperature. Indeed, as indicated in Fig. 16b, a peak in defect concentration is observed at 0.4 J/cm$^2$, a fluence that provides conditions of the maximum level of undercooling at the solidification front (Fig. 16a). At lower fluences, the maximum undercooling level is limited by the melting depth, while at higher fluences, the decreased level of point defects can be explained by the elevated temperature at the solid-liquid interface due to slower cooling rate.

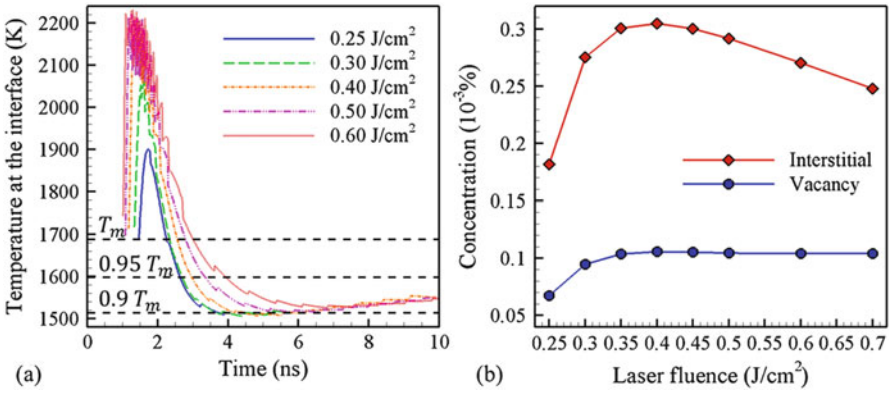


**Fig. 16** Evolution of temperature at the solid-liquid interface in the center of the laser spot on a Si target (**a**) and average concentrations of interstitials and vacancies in a region that experienced laser-induced melting and resolidification (**b**), as predicted by continuum-level simulations performed at different laser fluences. The laser pulse duration is 1 ns. In (**a**), the temperature profile ends when solidification is completed. The dashed lines mark the temperature levels of $T_m$, 0.95 $T_m$, and 0.9 $T_m$. The concentration of vacancies in (**b**) takes both individual vacancies and di-vacancies into account. The computational predictions on the concentrations of vacancies and interstitials generated at the rapidly advancing solidification front are used for informing the corresponding source terms in Eqs. 3, 4, and 5 of the continuum-level model, as described in the text. (The figures are adapted from Sun et al. in preparation)

## Thermal Annealing of Laser-Induced Crystalline Disorder in Silicon: Experiments and Simulations

The laser-induced crystalline disorder can deteriorate the performance of silicon-based devices due to the degradation of Si electrical properties. For example, the conversion efficiency of silicon solar cells can be dramatically decreased by the laser-induced amorphous phase that causes a high charge carrier recombination rate. It is necessary to minimize or eliminate the laser-induced disorder and retain the single-crystalline phase. The control of laser-induced disorder can be achieved through two approaches: minimization of laser-induced structural disorder by proper choice of laser-processing parameters and post-thermal annealing of the laser-induced disorder. With its ability to realize surface-selective heating, laser-based thermal annealing becomes a promising alternative to global annealing of the device. Moreover, laser annealing has an additional benefit of easy integration with the laser-based device fabrication process.

In the experimental section below, we focus on the demonstration of the ability of laser annealing to minimize the silicon surface disorder induced by laser processing and provide a brief discussion of the implementation of this method in the fabrication of silicon solar cells. Since it is difficult to obtain detailed information on the evolution of point defects in experiments, an analysis of the effect of laser parameters on the annealing efficiency is provided based on the results of continuum-level simulations.

### Experimental Studies on Thermal Annealing of Laser-Processed Si Devices

The use of conventional furnace and rapid thermal annealing (RTA) have been well studied over the last decades for making high-efficiency silicon solar cells and other electronic devices (Hartiti et al. 1994; Pecz et al. 2005; Li et al. 2013). Recently, laser-based thermal annealing has attracted considerable attention due to the selective, localized, and potentially cost-effective traits. The same laser setup used for processing can be applied to laser annealing (Fig. 3a).

In particular, laser annealing of the amorphous phase in ion-implanted or laser-processed silicon, as well as in amorphous silicon films deposited via chemical vapor deposition, has been explored (Thompson et al. 1984; Sun and Gupta 2016, 2018a; Qiu et al. 2014; Im et al. 1993). Thompson et al. (1984) and Im et al. (1993) have extensively analyzed the phase transformation mechanism activated by laser annealing that leads to crystallization of amorphous silicon in different laser fluence regimes. At high laser fluences, the amorphous silicon film/layer undergoes complete melting and follows the *l*-Si to *c*-Si transformation through the bulk nucleation and growth of c-Si nuclei (Stiffler et al. 1988). In the case of laser-processed silicon, the amorphous layer exists in direct contact with the underlying crystalline silicon, and an epitaxial growth of the crystalline phase usually occurs (Ouwens and Heijligers 1975). In contrast, at low laser fluences, the phase transformation is found to proceed through the explosive crystallization at c-Si/a-Si interface. In this

mechanism, the a-Si layer is partially melted near the surface and recrystallizes to the c-Si phase. The latent heat released in the crystallization of the surface region is conducted to the underlying layer and initializes the subsequent melting and regrowth process (Thompson et al. 1984; Im et al. 1993). Below the melting temperature, the relaxation of amorphous structure, with the decrease of bond angle spread and material densification, occurs at temperatures exceeding 250 °C, while the recrystallization starts above 500 °C (Yater 1992). Solid-state phase transformation is very slow, *i.e.*, ~0.03 nm/ns at 1300 °C (Stiffler et al. 1988), but this mechanism is still possible in microsecond or millisecond laser-based anneals.

The laser-induced annealing of crystalline defects in the ion-implanted silicon has been reported by Young et al. (Young et al. 1978; White et al. 1979) and Gat et al. (1978). The observations from these studies include the redistribution of dopant impurities and the recovery of crystallinity, as well as the improvement of electrical properties. The redistribution of dopants is attributed to the diffusion in the transient molten state. The dislocations, dislocation loops, and stacking faults can also be removed by laser annealing (Sun and Gupta 2016; White et al. 1979). The intrinsic point defects (vacancies and self-interstitials) are rarely investigated in terms of laser annealing. It is likely that interstitials could combine with vacancies and/or diffuse to the dislocation cores or the surface (Sun et al. in preparation). In general, the mechanisms involved in the laser annealing of crystal defects are still poorly understood and require further investigation.

For a wider acceptance of the laser-based technology in the emerging energy applications, laser annealing of the disorder and defects induced by the high-power laser processing has recently been investigated (Sun and Gupta 2016, 2018a). The effect of long pulse-duration (300 μs) IR laser annealing is found to be comparable with that of furnace annealing. The band-edge photoluminescence (Fig. 17a) is found to recover to the starting wafer value indicating the elimination of structural disorder. The laser annealing can also be used to induce migration of point defects. By comparing the attenuated total reflectance (ATR) spectra before and after the laser annealing (Fig. 17b), the interstitials and oxygen-vacancy complexes are shown to be nearly completely removed as a result of laser annealing. Even with a relatively short-pulse duration (50 ns) laser, an excellent charge carrier lifetime of 920 μs is achieved after laser annealing, which approaches the value of 1240 μs measured for the starting wafer (Fig. 17c) (Sun and Gupta 2016). A high charge carrier lifetime is critical for ensuring the carrier collection and, thus, a high conversion efficiency in Si-based photovoltaic applications. The recoveries of band-edge emission and carrier lifetime, as well as the disappearance of point-defect ATR absorbance, demonstrate that laser annealing can significantly reduce the levels of structural disorder and crystal defects in silicon samples.

A comparison of the results of laser annealing performed with different pulse durations shows that the annealing is most effective with long laser pulses, in the range of microseconds to milliseconds (Sun and Gupta 2018a). The irradiation with a short pulse duration can produce a relatively high peak power and may cause ablation in the center of the Gaussian beam, but it does not provide enough time for defect annihilation. The excessively long pulse duration or continuous-wave (CW) laser irradiation could lead to an undesired heating of the substrate.

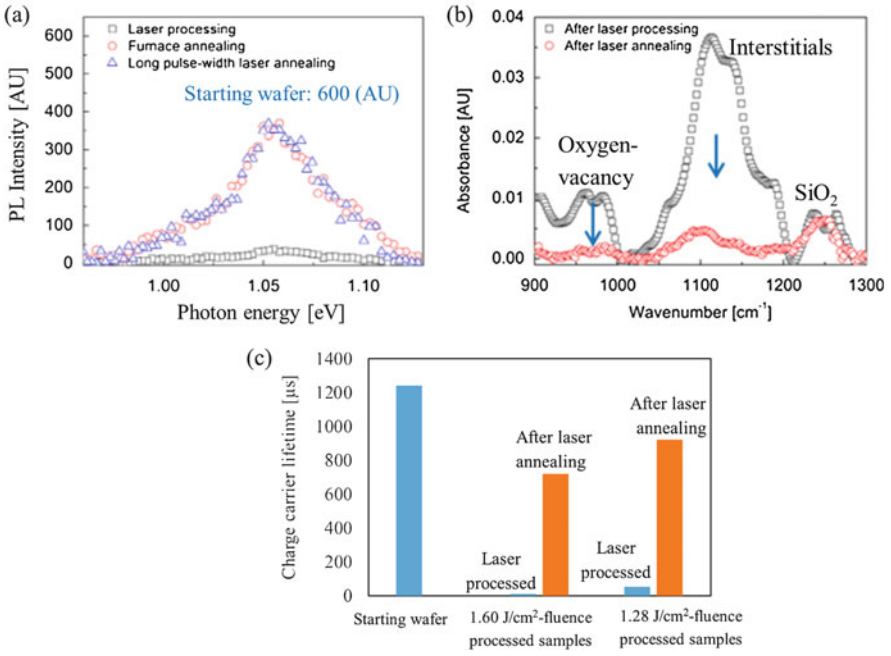


**Fig. 17** Demonstration of the use of laser annealing to minimize the surface disorder in laser-processed crystalline silicon. (**a**) Band-edge photoluminescence (PL) spectra after furnace or long-pulse duration (300 µs) laser annealing. (Reprinted from Sun and Gupta (2018a), with the permission of AIP Publishing). (**b**) Comparison of attenuated total reflectance (ATR) spectra before and after laser annealing (Sun et al. in preparation). (**c**) Charge carrier lifetime before and after 50 ns pulse laser annealing. (Reprinted from Sun and Gupta (2016), with permission from Elsevier)

The laser annealing technique has been applied to the transistor (Lee et al. 1979; Li et al. 2008; Zhang et al. 2006) and solar cell (Sun and Gupta 2018a) fabrication. In the case of transistors, the laser annealing is exploited to crystallize the amorphous silicon into polycrystalline silicon (Lee et al. 1979; Sera et al. 1989). Solar cell devices, which require a high charge carrier lifetime, are preferably reliant on single-crystalline silicon and are more sensitive to any disorder that might be introduced by laser processing. Figure 18a shows the device structure of all-laser-based IBC (interdigitated back contact) solar cells, which incorporate the laser doping and laser transferred metal contacts in the fabrication process (Sun and Gupta 2018a). With the laser annealing of this device, the disorder and defects induced by the laser doping are removed, and, thus, the carrier recombination near the junction is reduced, leading to an improvement of conversion efficiency (Fig. 18b). The metal/silicon interface disorder can be further reduced by performing annealing in a forming gas ambient.

Overall, the laser annealing process has been demonstrated to remove the laser-induced disorder, improve the crystalline quality of silicon, and, as a result, increase the charge carrier lifetime. This technique has also been demonstrated to enhance

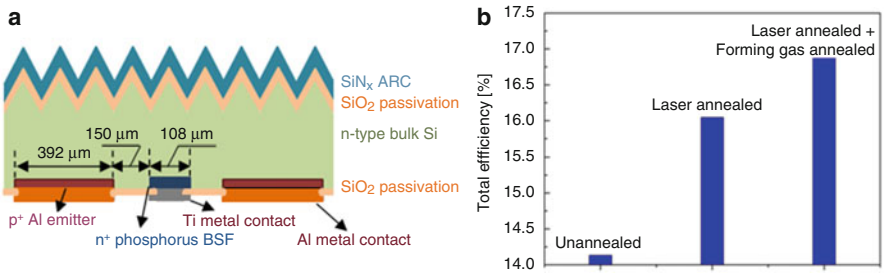


**Fig. 18** Demonstration of laser annealing to enhance the conversion efficiency of all-laser-based silicon IBC (interdigitated back contact) solar cells. (Reprinted from Sun and Gupta (2018a), with the permission of AIP Publishing). (**a**) Design structure. (**b**) Conversion efficiency comparison

laser-processed solar cell efficiency. With the progress in disorder removal, laser-based thermal annealing makes the low-cost, high-efficiency laser-processed silicon solar cell devices viable.

## Continuum Simulation of Laser Annealing of Point Defects

In section "Experimental Studies on Thermal Annealing of Laser-Processed Si Devices," the application of laser annealing for reducing the levels of point defect supersaturation has been demonstrated in experiments. In this section, the effect of parameters of laser annealing on the concentration of point defects is briefly discussed based on the results of a series of 1D continuum simulations. The continuum-level description of the evolution of point defects is given by Eqs. 3, 4, and 5 in section "Experimental and Computational Investigations of Laser-Induced Generation of Structural Defects in Silicon," excluding the source terms for the generation of nonequilibrium concentration of point defects at the solidification front. The system before the annealing is considered as a silicon target processed by a 1 ns laser pulse at 0.45 J/m$^2$, with the initial concentration of interstitials and vacancies taken from Fig. 15 at the laser spot center. The computational results on the effect of laser annealing performed with different values of laser fluence, pulse duration, and the number of pulses are plotted in Fig. 19. The concentration of point defects can be reduced through recombination of interstitials and vacancies, as well as by diffusion to the free surface or deeper into the bulk of the system, as described in Eqs. 3, 4, and 5. The irradiation conditions are selected to be below the melting threshold, so that the regeneration of nonequilibrium point defects upon the resolidification is avoided. The temperature generated by the laser irradiation should still be sufficiently high to maximize the recombination rates and diffusivity of the point defects during the laser annealing. The use of long pulse durations or irradiation by multiple pulses is also found to be beneficial, as the temporal window for effective annealing can be expanded in these cases. Overall, as shown in Fig. 19, the elimination of both interstitials and vacancies after the laser annealing becomes more efficient at higher laser fluences, longer pulse durations, and upon multi-pulse

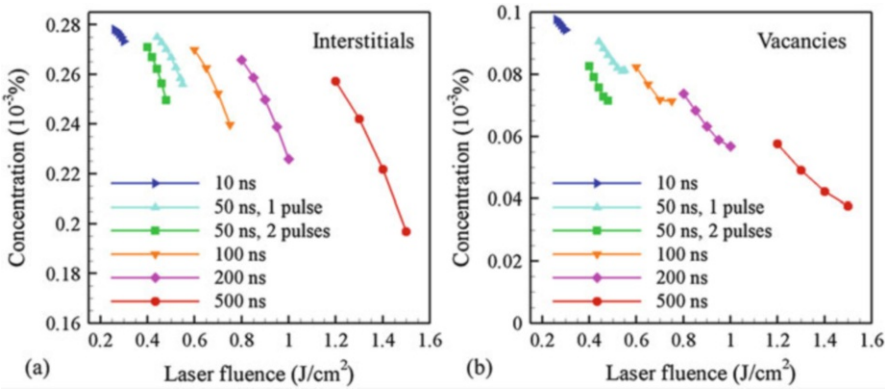


**Fig. 19** Average concentrations of interstitials (**a**) and vacancies (**b**) predicted in 1D continuum-level simulations of laser annealing. The vacancy concentrations include both individual vacancies and di-vacancies. The initial concentrations before the annealing are taken from the concentration profiles along the laser spot center predicted in a 2D simulation of laser melting and resolidification by a 1 ns laser pulse at 0.45 J/m$^2$ illustrated in Fig. 15. The concentrations are averaged over the melted depth along the laser spot center. (The figures are adapted from Sun et al. in preparation)

irradiation. The computational results indicate that a substantial reduction of the point defect concentration, down to the equilibrium concentration at the melting temperature, can be achieved with sub-microsecond laser irradiation slightly below the melting threshold. These computational predictions provide practical guidance for the selection of irradiation conditions in laser annealing applications.

## Summary

The laser-induced structural disorder, namely, the generation of amorphous phase, polycrystalline structure, and crystal defects, has been the subject of experimental and computational studies. Laser pulse duration, wavelength, and fluence play important roles in determining the thermodynamic and kinetic conditions required for amorphization. In the melting regime, short-pulse ($< 90$ ps) laser irradiation can lead to the formation of an amorphous phase due to high cooling rate during resolidification, whereas in the ablation regime, the amorphous phase can also be produced by nanosecond laser pulses. The short wavelength of the laser irradiation leads to the concentration of laser energy deposition in a very shallow surface layer (e.g., 10 nm for 266 nm wavelength) and tends to facilitate the amorphization due to steep temperature gradients and large cooling rates. The cooling rate and melt depth are also affected by laser fluence, which plays an important role in defining the degree of amorphization in laser processing.

Similar to amorphization, the laser-induced generation of crystal defects is sensitive to the irradiation parameters. In particular, experimental observations and computational predictions suggest that the maximum concentration of point defects is created at laser fluences between the melting and ablation thresholds, while

the dislocation density increases sharply with laser fluence in the ablation regime. Overall, the effect of the three irradiation parameters on amorphization and generation of crystal defects are intertwined and should be considered together in the analysis aimed at minimizing the laser-induced structural disorder.

The laser-based thermal annealing has also been investigated in modeling and experiments. The simulations predict that the mitigation of laser-induced point defects can be effective with multiple laser annealing pulses of longer duration. In experiments, the long pulse durations, in microsecond to millisecond range, are more effective in defect annihilation than shorter durations, while the excessively long pulses or continuous-wave laser irradiation usually causes undesired heating of the substrate. The laser annealing has been demonstrated to crystallize the amorphous silicon, redistribute the dopant impurities, and remove intrinsic point defects, dislocations, and stacking faults. Depending on laser annealing conditions, the crystallization of amorphous silicon may proceed through the epitaxial regrowth of the crystalline part of the sample, explosive crystallization, or solid-state phase transformation. The mechanistic analysis of laser-assisted removal of crystal defects requires more investigations, although the observation of the effective annealing has been widely reported. With the annealing of laser-induced disorder, the overall crystalline quality of laser-processed silicon can be restored together with the improvement of Si electrical properties, especially the charge carrier lifetime. As a result, the conversion efficiency of laser-based silicon photovoltaic devices can be greatly enhanced by integration of laser annealing into a general multistep laser processing procedure for electronic and optoelectronic device fabrication.

Finally, we note that while the review of laser-induced disorder and laser-based thermal annealing in this chapter is primarily focused on silicon, similar processes and trends have also been reported for other semiconductor materials.

## Cross-References


- ▶ Acoustic Emission and Ultrasound Monitoring in Laser Micro/Nanofabrication
- ▶ Bandgap Engineering of Quantum Semiconductor Microstructures
- ▶ Characterization of Laser-Processed Samples
- ▶ Laser Coupling and Relaxation of the Absorbed Energy: Metals, Semiconductors, and Dielectrics
- ▶ Laser-Induced Surface Modification for Photovoltaic Device Applications
- ▶ Laser-Induced Non-Thermal Processes
- ▶ Laser-Induced Periodic Surface Structures (LIPSS)
- ▶ Laser-Induced Thermal Processes: Heat Transfer, Generation of Stresses, Melting and Solidification, Vaporization, and Phase Explosion
- ▶ Microstructure Modification: Generation of Crystal Defects and Phase Transformations


**Acknowledgments** Financial support provided by the National Science Foundation (NSF) through Grants CMMI-1436775 and DMR-1610936 is gratefully acknowledged. We also thank the NSF IUCRC program, NASA Langley Professor Program, and the US Department of Energy's

Office of Energy Efficiency and Renewable Energy (EERE) under Solar Energy Technologies Office (SETO) Agreement Number DE-EE0007534 for their support. Z. Sun acknowledges Prof. Michael O. Thompson for valuable discussions.

## References

Amer MS, El-Ashry MA, Dosser LR, Hix KE, Maguire JF, Irwin B (2005) Femtosecond versus nanosecond laser machining: comparison of induced stresses and structural changes in silicon wafers. Appl Surf Sci 242:162

Ametowobla M, Bilger G, Kohler JR, Werner JH (2012) Laser induced lifetime degradation in p-type crystalline silicon. J Appl Phys 111:114515

Arora VK, Dawar AL (1996) Laser-induced damage studies in silicon and silicon-based photodetectors. Appl Opt 35:7061

Bergmann S, Albe K, Flegel E, Barragan-Yani DA, Wagner B (2017) Anisotropic solid-liquid interface kinetics in silicon: an atomistically informed phase-field model. Model Simul Mater Sci Eng 25:065015

Bernstein N, Aziz MJ, Kaxiras E (2000) Atomistic simulations of solid-phase epitaxial growth in silicon. Phys Rev B 61:6696

Bonse J, Baudach S, Kruger J, Kautek W, Lenzner M (2002) Femtosecond laser ablation of silicon–modification thresholds and morphology. Appl Phys A 74:19

Bonse J, Brzezinka KW, Meixner AJ (2004) Modifying single-crystalline silicon by femtosecond laser pulses: an analysis by micro Raman spectroscopy, scanning laser microscopy and atomic force microscopy. Appl Surf Sci 221:215

Bonse J, Kruger J, Hohm S, Rosenfeld A (2012) Femtosecond laser-induced periodic surface structures. J Laser Appl 24:042006

Bulgakova NM, Stoian R, Rosenfeld A, Hertel IV, Marine W, Campbell EEB (2005) A general continuum approach to describe fast electronic transport in pulsed laser irradiated materials: The problem of Coulomb explosion. Appl Phys A 81:345

Chang Z, Zhou N, Zhang C, Gong H, Lin M, Zhou L (2018) A molecular dynamics study of atomic configurations of dislocations accompanying twins in crystal growth of Si from melt. Model Simul Mater Sci Eng 26:085003

Cheng J, Liu C, Shang S, Liu D, Perrie W, Dearden G, Watkins K (2013) A review of ultrafast laser materials micromachining. Opt Laser Technol 46:88

Crawford THR, Yamanaka J, Botton GA, Haugen HK (2008) High-resolution observations of an amorphous layer and subsurface damage formed by femtosecond laser irradiation of silicon. J Appl Phys 103:053104

Crouch CH, Carey JE, Warrender JM, Aziz MJ, Mazur E, Genin FY (2004) Comparison of structure and properties of femtosecond and nanosecond laser-structured silicon. Appl Phys Lett 84:1850

Custer JS, Thompson MO, Jacobson DC, Poate JM, Roorda S, Sinke WC, Spaepen F (1994) Density of amorphous Si. Appl Phys Lett 64:437

Dahlinger M, Carstens K, Hoffmann E, Kohler JR, Zapf-Gottwick R, Werner JH (2017) 23.2% laser processed back contact solar cell: fabrication, characterization and modeling. Prog Photovolt 25:192

Gat A, Gibbons JF, Magee TJ, Peng J, Deline VR, Williams P, Evans CA Jr (1978) Physical and electrical properties of laser-annealed ion-implanted silicon. Appl Phys Lett 32:276

Green MA (2008) Self-consistent optical parameters of intrinsic silicon at 300 K including temperature coefficients. Sol Energy Mater Sol Cells 92:1305

Gupta VV, Song HJ, Im JS (1995) Non-equilibrium two-dimensional model of excimer-laser melting and solidification of thin Si films on $SiO_2$. MRS Proc 397:465

Haase F, Hollemann C, Schafer S, Merkle A, Rienacker M, Krugener J, Brendel R, Peibst R (2018) Laser contact opening for local poly-Si-metal contacts enabling 26.1%-efficient POLO-IBC solar cells. Sol Energy Mater Sol Cells 186:184

Halbwax M, Sarnet T, Delaporte Ph, Sentis M, Etienne H, Torregrosa F, Vervisch V, Perichaud I, Martinuzzi S (2008) Micro and nano-structuration of silicon by femtosecond laser: Application to silicon photovoltaic cells fabrication. Thin Solid Films 516:6791

Hameiri Z, Puzzer T, Mai L, Sproul AB, Wenham SR (2010) Laser induced defects in laser doped solar cells. Prog Photovolt 19:391

Hartiti B, Schindler R, Slaoui A, Wagner B, Muller JC, Reis I, Eyer A, Siffert P (1994) Towards high-efficiency silicon solar cells by rapid thermal processing. Prog Photovolt 2:129

He M, Zhigilei LV (in preparation) Computational study of phase transformations induced by short pulse laser irradiation of single crystalline silicon

He M, Wu C, Shugaev MV, Samolyuk GD, Zhigilei LV (2019) Computational study of short-pulse laser-induced generation of crystal defects in Ni-based single-phase binary solid-solution alloys. J Phys Chem C 123:2202–2215

Herrmann RFW, Gerlach J, Campbell EEB (1998) Ultrashort pulse laser ablation of silicon: an MD simulation study. Appl Phys A 66:35

Im JS, Kim HJ, Thompson MO (1993) Phase transformation mechanisms involved in excimer laser crystallization of amorphous silicon films. Appl Phys Lett 63:1969

Ishimaru M, Munetoh S, Motooka T, Moriguchi K, Shintani A (1998) Molecular-dynamics studies on defect-formation processes during crystal growth of silicon from melt. Phys Rev B 58:12583

Iyengar VV, Nayak BK, More KL, Meyer HM, Biegalski MD, Li JV, Gupta MC (2011) Properties of ultrafast laser textured silicon for photovoltaics. Sol Energy Mater Sol Cells 95:2745

Jackson KA (2002) The interface kinetics of crystal growth processes. Interface Sci 10:159

Jakse N, Pasturel A (2007) Liquid-liquid phase transformation in silicon: evidence from first-principles molecular dynamics simulations. Phys Rev Lett 99:205702

Jeschke HO, Garcia ME, Lenzner M, Bonse J, Kruger J, Kautek W (2002) Laser ablation thresholds of silicon for different pulse durations: theory and experiment. Appl Surf Sci 197–198:839

Jia J, Li M, Thompson CV (2004) Amorphization of silicon by femtosecond laser pulses. Appl Phys Lett 84:3205

Kisdarjono H, Voutsas AT, Solanki R (2003) Three-dimensional simulation of rapid melting and resolidification of thin Si films by excimer laser annealing. J Appl Phys 94:4374–4381

Lee KF, Gibbons JF, Saraswat KC, Kamins TI (1979) Thin film MOSFET's fabricated in laser-annealed polycrystalline silicon. Appl Phys Lett 35:173

Li R, Lee S, Hong M, Chi D, Kwong D (2008) Pt-germanide formed by laser annealing and its application for Schottky source/drain metal-oxide-semiconductor field-effect transistor integrated with TaN/chemical vapor deposition $HfO_2$/Ge gate stack. Jpn J Appl Phys 47:2548

Li W, Varlamov S, Dore J, Green M (2013) Defect annealing in ultra-thin polycrystalline silicon films on glass: rapid thermal versus laser processing. Mater Lett 107:1

Lin Z, Johnson RA, Zhigilei LV (2008) Computational study of the generation of crystal defects in a bcc metal target irradiated by short laser pulses. Phys Rev B 77:214108

Liu JM, Yen R, Kurz H, Bloembergen N (1981) Phase transformation on and charged particle emission from a silicon crystal surface, induced by picosecond laser pulses. Appl Phys Lett 39:755

Lu Q, Mao SS, Mao X, Russo RE (2008) Theory analysis of wavelength dependence of laser-induced phase explosion of silicon. J Appl Phys 104:083301

Luedtke WD, Landman U, Ribarsky MW, Barnett RN, Cleveland CL (1988) Molecular-dynamics simulations of epitaxial crystal growth from the melt. II. Si (111). Phys Rev B 37:4647

Mooney PM, Young RT, Karins J, Lee YH, Corbett JW (1978) Defects in laser damaged silicon observed by DLTS. Phys Status Solidi 48:K31

Motooka T, Munetoh S, Rishikawa R, Kuranaga T, Ogata T, Mitani T (2006) Molecular-dynamics simulations of recrystallization processes in silicon: nucleation and crystal growth in the solid-phase and melt. ECS Trans 3:207

Nagel H, Berge C, Aberle AG (1999) Generalized analysis of quasi-steady-state and quasi-transient measurements of carrier lifetimes in semiconductors. J Appl Phys 86:6218

Nishihira K, Motooka T (2002) Molecular-dynamics simulations of crystal growth from melted Si: Self-interstitial formation and migration. Phys Rev B 66:233310

Ohmer K, Weng Y, Kohler JR, Strunk HP, Werner JH (2011) Defect formation in silicon during laser doping. IEEE J Photovolt 1:183

Ouwens CD, Heijligers H (1975) Recrystallization processes in polycrystalline silicon. Appl Phys Lett 26:569

Pecz B, Dobos L, Panknin D, Skorupa W, Lioutas C, Vouroutzis N (2005) Crystallization of amorphous-Si films by flash lamp annealing. Appl Surf Sci 242:185

Qiu Y, Cristiano F, Huet K, Mazzamuto F, Fisicaro G, Magna AL, Quillec M, Cherkashin N, Wang H, Duguay S, Blavette D (2014) Extended defects formation in nanosecond laser-annealed ion implanted silicon. Nano Lett 14:1769

Rogers MS, Grigoropoulos CP, Minor AM, Mao SS (2009) Absence of amorphous phase in high power femtosecond laser-ablated silicon. Appl Phys Lett 94:011111

Sastry S, Angell CA (2003) Liquid-liquid phase transition in supercooled silicon. Nat Mater 2:739–743

Sera K, Okumura F, Uchida H, Itoh S, Kaneko S, Hotta K (1989) High-performance TFTs fabricated by XeCl excimer laser annealing of hydrogenated amorphous-silicon film. IEEE Trans Electron Devices 36:2868

Shank CV, Yen R, Hirlimann C (1983) Time-resolved reflectivity measurements of femtosecond-optical-pulse-induced phase transitions in silicon. Phys Rev Lett 50:454

Shugaev MV, He M, Lizunov SA, Levy Y, Derrien TJY, Zhukov VP, Bulgakova NM, Zhigilei LV (2018) Insights into laser-materials interaction through modeling on atomic and macroscopic scales. In: Ossi PM (ed) Advances in the application of lasers in materials science. Springer series in materials science, 274. Springer, Cham, p 107

Sinno T, Jiang ZK, Brown RA (1996) Atomistic simulation of point defects in silicon at high temperature. Appl Phys Lett 68:3028–3030

Sokolowski-Tinten K, Bialkowski J, von der Linde D (1995) Ultrafast laser-induced order-disorder transitions in semiconductors. Phys Rev B 51:14186

Stiffler SR, Thompson MO, Peercy PS (1988) Supercooling and nucleation of silicon after laser melting. Phys Rev Lett 60:2519

Sugioka K, Meunier M, Piqué A (2010) Laser precision microfabrication. Springer series in materials science. Springer, Berlin

Sun Z, Gupta MC (2016) Laser annealing of silicon surface defects for photovoltaic applications. Surf Sci 652:344

Sun Z, Gupta MC (2018a) A study of laser-induced surface defects in silicon and impact on electrical properties. J Appl Phys 124:223103

Sun Z, Gupta MC (2018b) Laser processing of silicon for photovoltaics and structural phase transformation. Appl Surf Sci 456:342

Sun Z, Deng X, Choi JJ, Gupta MC (2018) Silicon surface passivation by laser processing a sol–gel $TiO_x$ thin film. ACS Appl Energy Mater 1:5474

Sun Z, He M, Zhigilei LV, Gupta MC (in preparation) Laser-induced point defects in silicon: combined experimental and simulation investigations

Thompson MO, Mayer JW, Cullis AG, Webber HC, Chew NG, Poate JM, Jacobson DC (1983) Silicon melt, regrowth, and amorphization velocities during pulsed laser irradiation. Phys Rev Lett 50:896

Thompson MO, Galvin GJ, Mayer JW, Peercy PS, Poate JM, Jacobson DC, Cullis AG, Chew NG (1984) Melting temperature and explosive crystallization of amorphous silicon during pulsed laser irradiation. Phys Rev Lett 52:2360

Tom HWK, Aumiller GD, Brito-Cruz CH (1988) Time-resolved study of laser-induced disorder of Si surfaces. Phys Rev Lett 60:1438

Tsu R, Hodgson RT, Tan TY, Baglin JE (1979) Order-disorder transition in single-crystal silicon induced by pulsed UV laser irradiation. Phys Rev Lett 42:1356

Vonatsos KN, Pantelis DI (2005) Approximate solutions for the evaluation of the depth of laser-melted zones. Appl Phys A 80:885

Walter D, Fell A, Franklin E, Wang D, Fong K, Kho T, Weber K, Blakers AW (2015) Damage-free ultraviolet nanosecond laser ablation for high efficiency back contact solar cell fabrication. Sol Energy Mater Sol Cells 136:1

White CW, Narayan J, Young RT (1979) Laser annealing of ion-implanted semiconductors. Science 204:461

Wood RF (1981) Macroscopic theory of pulsed-laser annealing. I. Thermal transport and melting. Phys Rev B 23:2923

Yang C, Wang Y, Xu X (2012) Molecular dynamics studies of ultrafast laser-induced phase and structural change in crystalline silicon. Int J Heat Mass Transf 55:6060–6066

Yater JA (1992) Laser-induced amorphization and non-equilibrium solidification in silicon. Dissertation, Cornell University

Young RT, White CW, Clark GJ, Narayan J, Christie WH, Murakami M, King PW, Kramer SD (1978) Laser annealing of boron-implanted silicon. Appl Phys Lett 32:139

Young RT, Wood RF, Christie WH (1982) Laser processing for high-efficiency Si solar cells. J Appl Phys 53:1178

Zhang Q, Huang J, Wu N, Chen G, Hong M, Bera JK, Zhu C (2006) Drive-current enhancement in Ge n-channel MOSFET using laser annealing for source/drain activation. IEEE Electron Device Lett 27:728

Zhang S, Wang L-M, Zhang X, Qi L, Zhang S, Ma M, Liu R (2015) Polymorphism in glassy silicon: Inherited from liquid-liquid phase transition in supercooled liquid. Sci Rep 5:8590